

Constrained Random Phase Approximation: the spectral method

Merzuk Kaltak, Alexander Hampel, and Martin Schlipf
VASP Software GmbH, Berggasse 21/14, 1090 Vienna, Austria

Indukuru Ramesh Reddy and Bongae Kim
Department of Physics, Kyungpook National University, Daegu, 41566, Korea

Georg Kresse
*VASP Software GmbH, Berggasse 21/14, 1090 Vienna, Austria and
 Faculty of Physics and Center for Computational Materials Science,
 University of Vienna, Kolingasse 14-16, A-1090 Vienna, Austria
 (Dated: August 22, 2025)*

We present a new constrained Random Phase Approximation (cRPA) method, termed spectral cRPA (s-cRPA), and compare it to established cRPA approaches for Scandium and Copper by varying the 3d shell filling. The s-cRPA consistently yields larger Hubbard U interaction values. Applied to the realistic system CaFeO_3 , s-cRPA produces interaction parameters significantly closer to those required within $\text{DFT}+U$ to induce the experimentally observed insulating state, overcoming the metallic behavior predicted by standard density functionals. We also address the issue of negative interaction values found in the projector cRPA method for filled d-shells, demonstrating that s-cRPA offers superior numerical stability through electron conversion. Overall, s-cRPA is more robust and effectively overcomes the known underestimation of U in standard cRPA, making it a promising tool for the community. Additionally, we have enhanced our implementation with features for computing multi-center interactions to analyze spatial decay and developed a low-scaling variant with a compressed Matsubara grid to efficiently obtain full frequency-dependent interactions.

PACS numbers: 71.10.-w, 71.15.Mb, 71.20.Nr

Keywords: GW, DFT, PAW, RPA, c-RPA, cRPA, non-local RPA, p-cRPA, w-cRPA, Matsubara grid

I. INTRODUCTION

First principles methods are a cornerstone of modern theoretical physics and chemistry. Efficient first-principles methods often rely on conventional mean-field theories, such as Hartree-Fock or density functional theory (DFT) to describe material properties. However, for systems with partially filled narrow bands, i.e. systems with localized electrons in partially filled orbitals, these methods struggle to accurately describe the electron correlation effects beyond the static mean-field level. Such systems are often referred to as strongly correlated, and methods beyond static mean-field theory are necessary to accurately describe their physical properties.

In cases where the Hartree-Fock method and DFT fall short, model Hamiltonians that focus on a limited number of electrons near the Fermi level—so-called low-energy models—attempt to effectively capture the essential physics of strongly correlated matter. The application of model Hamiltonians to condensed matter physics began in the 1930s with the work of Slater and Bethe,^{1,2} followed by Mott’s contributions.³ Building upon Mott’s ideas, Hubbard developed an approach in 1963⁴ that continues to be extensively studied in the solid-state community.

The Hubbard model comprises two key components: a hopping term t , which describes the probability of strongly correlated electrons moving between sites, and a constant interaction term U , limited to interactions on

the same site. Despite its apparent simplicity compared to the full many-body Hamiltonian, the Hubbard model successfully describes various collective quantum phenomena, including the Mott transition, ferromagnetism, and the Kondo effect.^{5–8}

While an analytical solution for the Hubbard model with one electron in one spatial dimension can be obtained using the Bethe ansatz,^{2,9} explicit solutions for two or three dimensions remain elusive. The complexity of the model increases exponentially with the number of electrons, necessitating the use of sophisticated approximations to find numerical solutions with reasonable computational effort.

A significant advancement in this field occurred over two decades ago with the development of dynamical mean-field theory (DMFT), which considers the Hubbard model in the limit of infinite dimensions.¹⁰ DMFT is formulated in the Green’s function formalism, where instead of explicitly calculating the many-body wavefunction, the interacting single particle Green’s function is determined, which is directly related to photo-emission spectroscopy. Metzner and Vollhardt demonstrated that in this limit, all contributions to the interacting Green’s function vanish except for local Feynman diagrams, substantially reducing the complexity of the Hubbard model.¹¹ Subsequently, Kotliar and Georges showed that this model could be mapped onto an Anderson impurity model,¹² enabling the use of powerful quantum Monte Carlo techniques for numerical solutions.^{13–18}

These breakthroughs led to further investigations in

the field and the development of methods that incorporate advances in density functional theory, such as DFT+DMFT.^{19,20} DFT+DMFT combines the model aspects of DMFT with DFT, by constructing localized orbitals of a subset of Kohn-Sham (KS) orbitals for which the DMFT equations are solved. This combined method can also be derived formally from a general functional.²¹

Although the predictive power of DMFT is well-established,^{22–25} making the theory truly parameter-free or *ab initio* remains challenging. One particularly challenging aspect of DMFT is the choice of the effective one-center interaction, known as *Hubbard U*. For an isolated atom the Coulomb integrals are rather straightforward to compute. However, in a real solid the electrons of the constructed low-energy model interact with a much reduced Coulomb interaction that is screened by all other electrons in the system. This *U* is therefore a screened Coulomb interaction and is distinguished by the bare Coulomb interaction calculated from the overlap of the orbitals describing the model.

Cococcioni et al. introduced a linear response method for calculating the Hubbard *U* parameter from first principles, rather than fitting *U* empirically to experimental data.^{26–28} The method is consistent with the logic of DFT+*U*, but can lead to double counting issues in subsequent many-body treatments or to an overestimation for *U* for filled shells.²⁹

The development of the constrained random phase approximation (cRPA) marked a significant advancement in this field.^{30–32} cRPA divides the electronic system into two subsystems: one describing the correlated degrees of freedom dominant at the Fermi level (target or correlated space \mathcal{C}), and the rest space comprising the remaining Fock space, which acts as an effective medium screening the interaction between strongly correlated electrons near the Fermi surface.

In cRPA, all polarization effects between correlated electrons in the target space are eliminated to avoid double-counting perturbative contributions in subsequent model calculations. When the target states form an isolated manifold around the Fermi surface, this removal can be performed either directly in the plane wave basis³² or by solving a matrix equation in the Wannier domain.^{33,34}

However, more commonly, the target states are strongly entangled with non-correlated (s- or p-) states of the system, complicating the removal of screening effects in the correlated subspace. In such cases, careful separation of the target subspace \mathcal{C} from the rest of the system is necessary. Three cRPA schemes have been proposed to address this challenge. (i) The first method, known as disentangled cRPA³⁵, *disentangles* the states around the Fermi level, enabling a simpler removal of correlated polarizations in the Bloch domain.³⁶ This approach requires an energy window to project the Bloch functions around the Fermi surface onto a minimal basis set, resulting in effective interactions that depend on this choice.³⁶ (ii) The second approach, known as weighted cRPA (w-cRPA)

suggests including additional non-correlated (non-target) states in the Wannier basis to achieve a better representation of the Bloch states.^{37,38} Thus this approach aims at conserving the band structure. The effective interaction is calculated using a *weighted* polarizability, where the weights represent the probabilities of Bloch states being correlated. This approach has been developed by Şaşıoğlu et al.^{37,39} and implemented in various code packages.^{38,40–44} (iii) The third scheme, termed as projected cRPA (p-cRPA) method, can be derived from Kubo’s formalism⁴⁴ and has been applied in literature successfully as well.^{45–54} Typically, p-cRPA yields larger effective interactions compared to w-cRPA, because more screening effects are removed.

In the present work, we present a fourth method to calculate the partially screened Coulomb interaction for entangled target spaces. We will first recapitulate and analyse the similarities and differences between w-cRPA and p-cRPA, and then present a new scheme that remedies most of the shortcomings of the previously devised schemes. We call this method the spectral cRPA (s-cRPA) method and present its details in [II B 3](#).

The paper is structured as follows. Section [II](#) provides a brief overview of existing cRPA methods, where we give a short reminder about the details of w-cRPA and p-cRPA in [II B 1](#) and [II B 2](#), respectively. In Section [III](#), we compare the different cRPA schemes for fcc Sc and Cu, examining how the effective screened interaction evolves with the filling of the d shell. We then analyze the spatial decay and frequency dependence of the Hubbard *U*, and present results for the realistic compound CaFeO₃.

II. THEORY

A. Wannier functions and Hubbard model

Since the Hubbard model is based on the assumption of a local Coulomb interaction, a basis transformation of the delocalized Bloch states has to be performed to construct a low-energy model suitable to be solved by methods like DMFT. To this end, Wannier functions are typically leveraged. Wannier states are related to Bloch states through a combination of a unitary rotation *T* and a discrete Fourier transformation with respect to k-points⁵⁵

$$|w_{\alpha\mathbf{R}}\rangle = \frac{1}{N_{\mathbf{k}}} \sum_{n\mathbf{k}} e^{i\mathbf{k}\mathbf{R}} T_{\alpha n}^{(\mathbf{k})} |\phi_{n\mathbf{k}}\rangle. \quad (1)$$

It will be convenient to work with the mixed basis representations, also known as analytic *quasi-Bloch* states⁵⁶

$$|w_{\alpha\mathbf{k}}\rangle = \sum_n T_{\alpha n}^{(\mathbf{k})} |\phi_{n\mathbf{k}}\rangle. \quad (2)$$

It is important to note the arbitrary nature of the Wannier transform, since for each Bloch state the phase factors can be arbitrarily chosen.^{55,57} Marzari

and Vanderbilt proposed a maximally localized scheme, which chooses the phases to minimize a spread functional to produce maximally localized Wannier functions (MLWFs).^{58,59} This approach aims to maximize the spatial localization of the Wannier functions. However, in practical applications often so-called *first guess*⁶⁰ Wannier functions are employed, in which the rotation in Eq.(1) is defined as:

$$T_{\alpha n}^{(\mathbf{k})} = \langle \phi_{n\mathbf{k}} | Y_{\alpha} \rangle, \quad (3)$$

where $|Y_{\alpha}\rangle$ indicates e.g. eigenfunctions of the hydrogen atom. An additional orthonormalization of the resulting orbitals is performed. The preference for Eq. (3) is due to its tendency to produce Wannier functions that respect symmetries of the system, whereas MLWFs often break the symmetry. In case of entangled bands (crossing bands in the Brillouin zone), another crucial step is the disentanglement of the Wannier functions. The disentanglement procedure is performed before the orthonormalisation and maximally localisation procedures, in order to optimise the KS states in the chosen target space and ensure that the eigenvalues vary smoothly. In this study, we exclusively consider Wannier functions obtained from first guesses (but including disentanglement) for easier comparability with other studies.

The main focus of this paper is the model Hamiltonian

$$H = \sum_{\bar{\alpha}\bar{\beta}} t_{\bar{\alpha}\bar{\beta}} c_{\bar{\alpha}}^{\dagger} c_{\bar{\beta}} + \sum_{\bar{\alpha}\bar{\beta}\bar{\gamma}\bar{\delta}} U_{\bar{\alpha}\bar{\beta}\bar{\gamma}\bar{\delta}} c_{\bar{\alpha}}^{\dagger} c_{\bar{\beta}}^{\dagger} c_{\bar{\delta}} c_{\bar{\gamma}}, \quad (4)$$

where the compact notation $\bar{\alpha} = (\alpha, \mathbf{R}_{\alpha})$ has been introduced and the sum in the second term is restricted to the same unit cell $R_{\alpha} = R_{\beta} = R_{\gamma} = R_{\delta}$. The first term $t_{\bar{\alpha}\bar{\beta}}$ describes the electron hopping from the Wannier state $|w_{\bar{\alpha}}\rangle$ to state $|w_{\bar{\beta}}\rangle$ between the real lattice site \mathbf{R}_{α} and \mathbf{R}_{β} . These matrix elements are obtained by evaluating the Kohn-Sham Hamiltonian in the Wannier basis given by the transformation in Eq. (3). For further information see also Ref. 61. It is common practice in DMFT to treat the hopping between two different sites, as well as the Coulomb interaction between sites on the mean field level, using for instance, density functional theory or another simplified theory such as GW.

B. Coulomb interaction and cRPA

We focus our attention on the determination of the second term $U_{\alpha\beta\gamma\delta}$ located at $\mathbf{R} = \mathbf{0}$. This term describes the effective interaction between two electron-hole pairs $|w_{\alpha}, w_{\beta}\rangle, |w_{\delta}, w_{\gamma}\rangle$ and can be approximated as the expectation value of an effectively screened Coulomb kernel \mathbf{U} ⁴³ at zero frequency

$$U_{\alpha\beta\gamma\delta} = \langle w_{\alpha}, w_{\beta} | \mathbf{U}(\omega = 0) | w_{\delta}, w_{\gamma} \rangle. \quad (5)$$

In this paper, we study and require only the on-site *Hubbard-Kanamori* interaction⁴³

$$U = \frac{1}{N} \sum_{\alpha=1}^N U_{\alpha\alpha\alpha\alpha}. \quad (6)$$

Here, N is the number of correlated states that span the target subspace \mathcal{C} . This space is described by the Hamiltonian (4) and consists typically of d-states localized on specific atoms in the unit cell.

In cRPA the effective kernel \mathbf{U} is obtained formally from the effective polarizability

$$\chi^r(\omega) = \chi(\omega) - \chi^c(\omega) \quad (7)$$

and the bare Coulomb interaction \mathbf{V} via³¹

$$\mathbf{U}(\omega) = \mathbf{V} + \mathbf{V} \chi^r(\omega) \mathbf{U}(\omega). \quad (8)$$

The effective polarizability χ^r contains all polarization effects at the RPA level (described by χ), except those within the correlated space \mathcal{C} . These contributions are described by the correlated part χ^c .³¹

We emphasize that this separation is trivial in the Bloch domain only if the target space \mathcal{C} forms an isolated set of bands known as composite band.⁵⁶ In this case, it is always possible to find a minimal Wannier basis.⁵⁶ For these systems, the effective time-ordered polarizability takes the constrained form of the Adler and Wiser expression^{62,63}

$$\begin{aligned} \chi_{\mathbf{G}\mathbf{G}'}^c(\mathbf{q}, \omega) &= \frac{1}{N_{\mathbf{k}}} \sum_{\mathbf{k}} \sum_{n, n' \in \mathcal{C}} \frac{(1 - f_{n\mathbf{k}}) f_{n'\mathbf{k}+\mathbf{q}}}{\epsilon_{n\mathbf{k}} - \epsilon_{n'\mathbf{k}+\mathbf{q}} - \omega \mp i\eta} \\ &\langle \phi_{n\mathbf{k}} | e^{i(\mathbf{G}+\mathbf{q})\mathbf{r}} | \phi_{n'\mathbf{k}+\mathbf{q}} \rangle \\ &\langle \phi_{n'\mathbf{k}+\mathbf{q}} | e^{-i(\mathbf{G}'+\mathbf{q})\mathbf{r}'} | \phi_{n\mathbf{k}} \rangle, \end{aligned} \quad (9)$$

where \mathbf{G}, \mathbf{G}' are reciprocal lattice vectors, $N_{\mathbf{k}}$ the number of \mathbf{k} -points in the first Brillouin zone, $f_{n\mathbf{k}}$ the occupancies of the Bloch state $\phi_{n\mathbf{k}}$ having the energy $\epsilon_{n\mathbf{k}}$ and the shorthand $\mp i\eta = -i\eta \operatorname{sgn}(\epsilon_{n\mathbf{k}} - \epsilon_{n'\mathbf{k}+\mathbf{q}})$ was used. In this simple case, χ^r includes all transitions but those where the occupied and filled states are both in the isolated set of bands. Since the isolated set of bands is well defined, the procedure is well defined.

However, the correlated states are often found to be entangled with other non-correlated ones. As a result, the subspace \mathcal{C} , described by the model Hamiltonian (4), can only be defined in the localized Wannier basis in most cases. The corresponding expression for the effective polarizability χ^c is thus also well defined only in the Wannier basis

$$\begin{aligned} \chi^c(\mathbf{r}, \mathbf{r}', \omega) &= \frac{1}{N_{\mathbf{k}}^2} \sum_{nn' \mathbf{k}\mathbf{k}'} \sum_{\bar{\alpha}\bar{\beta}\bar{\gamma}\bar{\delta} \in \mathcal{C}} \frac{(1 - f_{n\mathbf{k}}) f_{n'\mathbf{k}'}}{\epsilon_{n\mathbf{k}} - \epsilon_{n'\mathbf{k}+\mathbf{q}} - \omega \mp i\eta} \\ &T_{\bar{\alpha}n}^{*(\mathbf{k})} T_{\bar{\beta}n'}^{(\mathbf{k}')} w_{\bar{\alpha}}^*(\mathbf{r}) w_{\bar{\beta}}(\mathbf{r}) w_{\bar{\gamma}}^*(\mathbf{r}') w_{\bar{\delta}}(\mathbf{r}') T_{\bar{\gamma}n'}^{*(\mathbf{k}')} T_{\bar{\delta}n}^{(\mathbf{k})} \end{aligned} \quad (10)$$

and follows from Kubo's expression⁴⁴

$$\chi^c(\mathbf{r}, \mathbf{r}', t) = -i \langle \mathcal{T} [\delta n_c(\mathbf{r}, t) \delta n_c(\mathbf{r}', 0)] \rangle_0, \quad (11)$$

where \mathcal{T} indicates the Dyson time-ordering operator and δn_c the correlated fluctuation density operator measured with respect to the non-interacting ground state.^{64,65}

In practice, neither Eq. (11) nor Eq. (10) proves to be practical. The former is overly formal and abstract, whereas the latter is computationally intractable. Consequently, it is preferable to reformulate χ^c in reciprocal space. A convenient way to find this expression is presented in the appendix A. Here we report only the final result

$$\begin{aligned} \chi_{\mathbf{G}\mathbf{G}'}^c(\mathbf{q}, \omega) = & \frac{1}{N_{\mathbf{k}}} \sum_{nn'\mathbf{k}} \frac{(1 - f_{n\mathbf{k}})f_{n'\mathbf{k}+\mathbf{q}}}{\epsilon_{n\mathbf{k}} - \epsilon_{n'\mathbf{k}+\mathbf{q}} - \omega \mp i\eta} \\ & \langle \bar{\phi}_{n\mathbf{k}} | e^{i(\mathbf{q}+\mathbf{G})\mathbf{r}} | \bar{\phi}_{n'\mathbf{k}+\mathbf{q}} \rangle \\ & \langle \bar{\phi}_{n'\mathbf{k}+\mathbf{q}} | e^{-i(\mathbf{q}+\mathbf{G}')\mathbf{r}'} | \bar{\phi}_{n\mathbf{k}} \rangle \end{aligned} \quad (12)$$

which contains the correlated Bloch functions and projectors

$$| \bar{\phi}_{n\mathbf{k}} \rangle = \sum_m P_{nm}^{(\mathbf{k})} | \phi_{m\mathbf{k}} \rangle \quad (13)$$

$$P_{nm}^{(\mathbf{k})} = \sum_{\alpha \in \mathcal{C}} T_{n\alpha}^{*(\mathbf{k})} T_{\alpha m}^{(\mathbf{k})}. \quad (14)$$

Unfortunately, there is a problem with the definiteness of polarizability χ^r using the procedures outlined above. This is mostly clearly seen by inspecting the long-wave length limit of the polarization, i.e. the value at $\mathbf{q} \rightarrow 0$. To evaluate this, the standard approach is k-p perturbation theory, which yields for the long-wave limit the following contribution⁶⁶

$$\lim_{\mathbf{q} \rightarrow 0} \frac{\chi(\mathbf{q}, \omega)}{|\mathbf{q}|^2} = \frac{1}{N_{\mathbf{k}}} \sum_{nm\mathbf{k}} \frac{(1 - f_{n\mathbf{k}})f_{m\mathbf{k}}}{\epsilon_{n\mathbf{k}} - \epsilon_{m\mathbf{k}} - \omega \mp i\eta} |\mathbf{O}_{nm}^{(\mathbf{k})}|^2. \quad (15)$$

If \mathbf{H} denotes the KS Hamiltonian and \mathbf{S} the overlap operator the optical transition elements can be written as⁶⁷

$$\begin{aligned} \mathbf{O}_{nm}^{(\mathbf{k})} &= \langle \phi_{n\mathbf{k}} | \nabla_{\mathbf{k}} \phi_{m\mathbf{k}} \rangle \\ &= \frac{\langle \phi_{n\mathbf{k}} | \nabla_{\mathbf{k}} (\mathbf{H} - \mathbf{S}\epsilon_{m\mathbf{k}}) | \phi_{m\mathbf{k}} \rangle}{\epsilon_{n\mathbf{k}} - \epsilon_{m\mathbf{k}}} \end{aligned} \quad (16)$$

In practice, terms with transition energies below a certain threshold in Eq. (15) as well as in Eq. (16) are neglected. This is a robust approach for the fully screened interaction, but can be problematic when extending the long-wave limit to cRPA. To describe the $q \rightarrow 0$ limit in cRPA requires the subtraction of

$$\bar{\mathbf{O}}_{nm}^{(\mathbf{k})} = \sum_{n', m'} P_{n, n'}^{*(\mathbf{k})} \mathbf{O}_{n' m'}^{(\mathbf{k})} P_{m' m}^{(\mathbf{k})} \quad (17)$$

from the fully-screened term (15).

Unfortunately, the Wannier projection's disentanglement

procedure modifies the \mathbf{k} -dependent wavefunction behavior at band crossings (prohibited crossings), such that often more screening terms are subtracted from Eq. (15). That is, the positivity condition

$$|\bar{\mathbf{O}}_{nm}^{(\mathbf{k})}|^2 \leq |\mathbf{O}_{nm}^{(\mathbf{k})}|^2 \quad (18)$$

can be violated for bands in the correlated subspace that are subject to Wannier projection. The result are negative definite dielectric functions, and with that negative cRPA interactions at zero frequency.

This undermines the method's reliability and is the main reason why several approximations were proposed in the community, which we summarize in the following. Finally, we also present a new scheme: s-cRPA that remedies most of the shortcomings of the devised schemes.

1. Weighted method: w-cRPA

The scheme of Şaşıoğlu et al., known as w-cRPA,⁵² follows from Eq. (12) using^{37,38}

$$P_{nm}^{(\mathbf{k})} \approx \sqrt{P_{nn}^{(\mathbf{k})}} \delta_{nm}. \quad (19)$$

The diagonal of the projectors measures the *correlation degree* of all Bloch bands that contribute to the Wannier states at a specific k-point and can be understood in terms of the statistical leverage score for band n .

The statistical leverage measures how *outlying* a row is with respect to the span N of the matrix.⁶⁸ More precisely, the leverage score of row n of P is defined via

$$l_n = \|v_n\|_N^2, \quad 0 \leq l_n \leq 1, \quad (20)$$

where v_n is the n -th singular eigenvector of P and the norm is computed over the first N dimensions of v_n , corresponding to the span of P .⁶⁹ These vectors constitute the columns of the unitary matrix V in the singular value decomposition $P = U\Sigma V^\dagger$. In the appendix B we show that $l_n = P_{nn}$ holds true at each k-point.

The w-cRPA method has two favorable properties. First, the positivity condition (18) is never violated; the leverage is a positive number between 0 and 1. Second, w-cRPA conserves the number of electrons, because the trace of the projectors remains unchanged by the approximation (19).

Nevertheless, the robustness of the method comes with a caveat. Screening effects inside the correlated subspace described by the off-diagonal terms of the correlated projectors (14) are not removed from the fully screened polarizability in w-cRPA. The interaction in resulting model Hamiltonians is often too weak to describe important phase transitions.^{52,70} A cRPA method that takes off-diagonal components of the projectors (14) into account and thus removes more screening effects from the correlated subspace is discussed in the following.

2. Projector method: p-cRPA

From the discussion at the end of section II B one concludes that preserving the positivity condition (18) without neglecting screening effects, that is, off-diagonal components in the correlated projectors (14), are conflicting goals. To solve this dilemma at least partially, one can sacrifice electron conservation and delete almost linearly dependent entries in P . It can be expected that almost linearly-dependent correlated Bloch states are close in energy and thus the main reason for the violation of (18). In p-cRPA, these vectors are identified as the zeros of the eigenvalues Θ_n of the projector after a Jacobi diagonalization^{71,72}

$$P_{nm}^{(\mathbf{k})} \approx \Theta_n^{(\mathbf{k})} P_{nm}^{(\mathbf{k})}. \quad (21)$$

It has been shown that the regularization (21) improves the robustness of Eq. (12) significantly when combined with the long-wave limit (15) and (17).⁴⁴

The eigenvalue ordering of the employed diagonalization algorithm closely follows the value of the leverage; columns with the smallest leverage are removed. However, the ordering is not always exact, especially for dense k-point meshes it often fails to select the Bloch bands with highest leverage score. Imposing strict ordering and selecting columns with highest leverage score gives rise to a revised version of p-cRPA, called p-cRPA-rev in the following.

Both methods, p-cRPA and p-cRPA-rev remove more screening effects compared to w-cRPA, because off-diagonal terms in the projector are present, even after regularization. Unfortunately, there are cases where this regularization still introduces negative long-wave limits as demonstrated in Fig. 5 of section III. In such cases, positive definite interactions are only obtained for very dense k-point samplings. We suspect that the origin of this problem stems from the fact that electron conservation is violated, i.e. the trace of the projector is not conserved after regularization.

3. Spectral method: s-cRPA

To remedy the drawbacks of p-cRPA and w-cRPA we propose to use the spectrum of the original projectors (14)

$$P_{nm}^{(\mathbf{k})} \approx \Theta_n^{(\mathbf{k})} \delta_{nm}, \quad (22)$$

ordered by the leverage (20). We denote this method in the following as spectral cRPA or s-cRPA due to its connection to the eigenspectrum of the original projector.

This cRPA scheme is a mixture of w-cRPA and p-cRPA(-rev) with altered weights (19) that includes also information about off-diagonal components of the original projectors. Since the trace of Eq. (22) is conserved (as for w-cRPA), the corresponding long-wave limit is

strictly positive definite; a fact that we also observed for all our calculations reported in the section (III).

The scheme suggested here is conceptually exceedingly simple. Eq. (22) either includes a specific Bloch state in the calculation of the polarizability of the correlated subspace, or it entirely neglects a state. At each k-point, the same number of N target states is selected (typically $N = 5$ states for d-electrons). The key differentiator of the present method is that the choice of whether a state is included or not is solely based on the leverage score; only Bloch states are selected that involve the strongest contribution from Wannier orbitals, and Bloch states that involve the weakest contribution of Wannier states are neglected. This is in the spirit of the CUR rank compression.⁷³ That is, one does not seek a linear combination of states (as done for instance, in singular value decompositions), but rather selects at each k-point the most relevant active Bloch states. It should be clear that this simply removes contributions from the full polarizability that were initially included. Hence, positive definiteness of the residual polarizability is guaranteed. Furthermore, the number of states is exactly conserved. Despite its simplicity, we will show below that the results of this method follow all expected trends, and the method also leads to fast k-point convergence.

C. Computational details

We have examined the effective interaction for Scandium (Sc) and Copper (Cu) in face-centered cubic (fcc) lattices with lattice constants of 4.64 Å and 3.52 Å, respectively. Given the metallic nature of these systems, Brillouin zone integration can be challenging, particularly when flat and partially occupied bands are present. To address this issue, we employed a methodological approach that involved determining the ground state wavefunction and the long-wave limit (15) using a dense k-point grid of $24 \times 24 \times 24$ points with a smearing factor of $\sigma = 0.1$ eV⁻¹. The same k-point grid was utilized for the Wannier projection, while a coarser grid of $8 \times 8 \times 8$ points was employed during the cRPA step. This k-point grid was also used for the determination of the spatial decay of U up to 14 Å.

To achieve convergence of the effective interaction matrix with respect to the plane wave basis set, we followed the method described in Ref. 34. This approach involves determining the effective matrix elements using a low energy cutoff $E_{\text{cut}}^{\text{low}}$ for the cRPA polarizability χ^r on a plane wave grid using shape restoration of the density.⁷⁴ The result is corrected by the difference between the bare Coulomb interaction matrix obtained with the same technique and the one obtained using exact one-centre terms for the charge density with a higher cutoff $E_{\text{cut}}^{\text{high}}$. This correction is justified because high-energy contributions to the polarizability χ^r vanish, and screening becomes ineffective for large \mathbf{G} vectors.

Specifically, we used $E_{\text{cut}}^{\text{low}} = 400$ eV for the cRPA po-

larizability, $E_{\text{cut}}^{\text{high}} = 700$ and $E_{\text{cut}} = 500$ eV for the PAW basis set. Similar to *GW* calculations, all bands provided by the plane wave cutoff are included in cRPA calculations. For our chosen settings, this corresponded to 288 bands for the transition metals.

We also explored the use of a mixed stochastic-deterministic compression algorithm to reduce the number of bands.⁷⁵ We employed a constant energy ratio of $F = 0.04$, with $N_p = 32$ protected bands and two stochastic bands per pseudo state ($N_\xi = 2$), resulting in a total of 106 bands. This approach achieved a speed-up of approximately 50 per cent for the cRPA calculations while incurring a negligible error of less than 50 meV in the effective interaction matrix. However, we found that naive truncation of the basis set without any compression yielded a similar level of error. Consequently, we recommend avoiding this compression for most cRPA calculations, except perhaps for very challenging (almost norm-conserving) pseudopotentials.

All results have been obtained within the finite-temperature formalism of many-body perturbation theory on the imaginary frequency axis. For this purpose, a compressed Matsubara grid has been determined by preserving the isometry of the time and frequency representations of Green's functions in $\text{NOMEGA}=24$ dimensional subspaces.⁷⁶ Typically, half as many points suffice to determine the static effective interaction. However, doubling the number of points is helpful to reconstruct details of the real-frequency interactions using a Padé fit of the data on the imaginary axis. For this purpose, we have applied the adaptive Antoulas-Anderson (AAA) algorithm⁷⁷ as interfaced in `py4vasp`.⁷⁸

III. RESULTS

A. Wannier basis for Sc and Cu

The effectiveness of the cRPA calculations is significantly influenced by the quality of the Wannier basis. For 3d transition metals, the absence of an isolated set of bands precludes a bijective mapping between Bloch bands and Wannier functions. Nevertheless, an approximate one-to-one correspondence can be established between six Wannier states and six bands in the vicinity of the Fermi level. These bands comprise five narrow bands, predominantly of d-character, and one itinerant band capturing the 4s orbital.

In our study, we positioned the s-like Wannier state at the direct coordinates (0.25, 0.25, 0.25), while the d-states were centered on the transition metal atom at the origin. Figure 1 illustrates a comparison between the original Kohn-Sham bands and the eigenvalues of the Hamiltonian in the Wannier basis for both Sc and Cu. The Wannier basis demonstrates high accuracy in reproducing most symmetry lines; however, it encounters difficulties in representing the high symmetry points W and K of the s-state. This limitation arises from these points

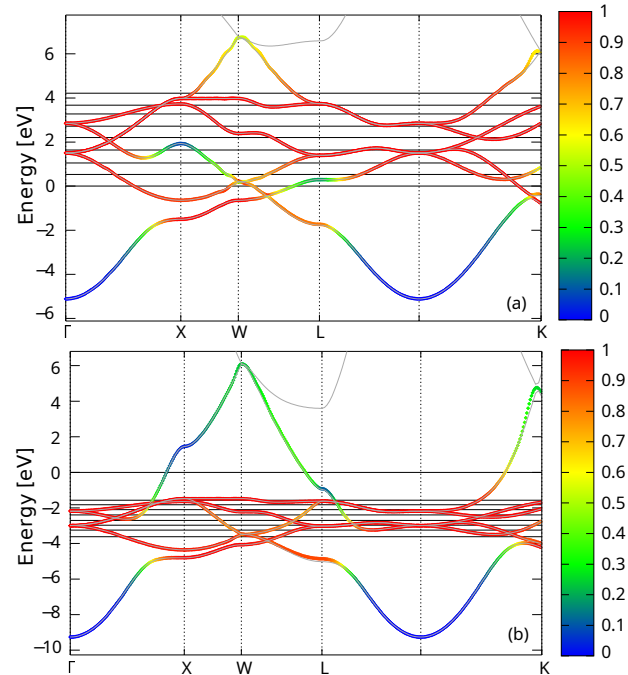


FIG. 1: Bands of fcc Sc (a) and Cu (b) with d-character resolution obtained from `Wannier90`.⁶⁰ Red bands indicate strong d-character, blue bands indicate strong s-character. For reference, the original band structure obtained with `VASP`⁷⁹ is shown in gray. Filling levels are indicated by horizontal lines (neutral compound at zero energy).

being intersections with higher energy states, which are not considered in our Wannier basis. Consequently, the eigenvalues of the Wannier Hamiltonian exhibit oscillatory behavior at these points.

Given that the representability of the Wannier basis is inherently imperfect, we implemented a very dense k-point grid of $24 \times 24 \times 24$ for the Wannier projection to allow the aforementioned disentanglement of states in the Wannier construction to work optimally.

B. Electron filling and Hubbard U

To evaluate the impact of the cRPA methods at various electron fillings, we maintained a consistent Wannier projection while adjusting the electron number—increasing it for Sc and decreasing it for Cu. In Table I and Table II we present the effective averaged on-site interaction U (see Eq. 6) in eV for Sc and Cu at different fillings.

Additionally, we analyzed the quotient U/W , where W represents the fully screened Hubbard-Kanamori interaction. This approach allows us to isolate and compare the unscreening effect of each method without incorporating Wannier localization effects. The results of this comparison are presented in Figure 2.

For all calculations the s-cRPA gives the largest interactions across all fillings both for Sc and Cu. The p-cRPA and p-cRPA-rev methods produce intermediate

TABLE I: Effective averaged on-site interaction U (see Eq. 6) in eV for Sc at different fillings, comparing the different disentanglement schemes presented in Sec. II B.

| cRPA | Sc | Sc ⁻ | Sc ²⁻ | Sc ³⁻ | Sc ⁴⁻ | Sc ⁵⁻ | Sc ⁶⁻ | Sc ⁷⁻ | Sc ⁸⁻ |
|-------|-----|-----------------|------------------|------------------|------------------|------------------|------------------|------------------|------------------|
| w | 2.4 | 2.3 | 2.3 | 2.6 | 2.6 | 2.6 | 2.4 | 2.1 | 1.9 |
| p | 2.2 | 1.9 | 2.0 | 2.4 | 2.7 | 2.8 | 2.6 | 2.5 | 2.2 |
| p-rev | 2.2 | 1.9 | 2.0 | 2.4 | 2.7 | 2.8 | 2.6 | 2.4 | 2.1 |
| s | 2.6 | 2.4 | 2.6 | 2.8 | 3.0 | 3.0 | 2.8 | 2.6 | 2.4 |

TABLE II: Effective averaged on-site interaction U (see Eq. 6) in eV for Cu at different fillings, comparing the different disentanglement schemes presented in Sec. II B. (°) values obtained from extrapolation without long-wave limit, see Fig. 5.

| cRPA | Cu ⁺⁸ | Cu ⁺⁷ | Cu ⁺⁶ | Cu ⁺⁵ | Cu ⁺⁴ | Cu ⁺³ | Cu ⁺² | Cu ⁺ | Cu |
|-------|------------------|------------------|------------------|------------------|------------------|------------------|------------------|-----------------|------|
| w | 3.3 | 3.0 | 2.8 | 2.9 | 3.2 | 3.4 | 3.5 | 3.6 | 4.7 |
| p | 4.2 | 4.2 | 4.3 | 4.6 | 4.9 | 4.8 | 4.6 | 4.2 | 4.3° |
| p-rev | 4.5 | 4.4 | 4.4 | 4.6 | 4.7 | 4.5 | 4.2 | 3.8 | 4.3° |
| s | 5.3 | 5.5 | 5.5 | 5.4 | 5.2 | 4.9 | 4.5 | 4.1 | 4.1 |

results, often very close to each other. This similarity demonstrates that the employed Jacobi diagonalization method effectively orders the eigenvalues according to the N -dimensional leverage score.

All methods exhibit their maximum effect roughly at half-filling, which is expected due to the prevalence of intra d-d transitions that are removed from screening. The maximum is more pronounced for Sc compared to Cu, likely due to the greater localization of d-states in Cu. The latter is also the reason for the overall larger interaction values compared to the Sc series.

Figure 2 illustrates that s-cRPA removes most intra-d screening effects, more so than p-cRPA and p-cRPA-rev. This difference is attributed to the electron number conservation in s-cRPA, which is not maintained in the regularization scheme employed in p-cRPA. Both p-cRPA(rev) and s-cRPA implicitly consider off-diagonal elements of the correlated projector, whereas w-cRPA neglects these contributions, resulting in the smallest interactions overall.

C. Frequency dependence

Next, we focus on the frequency dependence of the effective one-site interaction for Sc⁴⁺. Figure 3 shows U as a function of the frequency ω for s-cRPA, w-cRPA and p-cRPA obtained from analytic continuation of the compressed Matsubara data to the real axis (solid lines).⁷⁶ For comparison real-frequency data obtained from direct, pointwise calculation is also shown (dashed lines). As can be seen, reconstruction of real-frequency data is excellent, including the plasmon peak around 20 eV. Even unique features, such as the peak of p-cRPA around 4.5 eV are

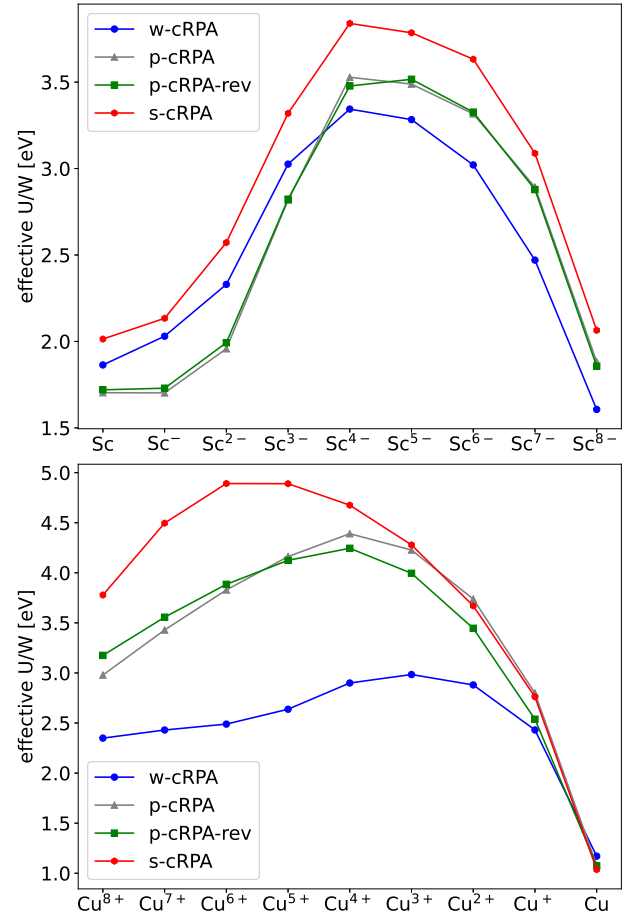


FIG. 2: Comparison of the quotient of on-site effective d-Coulomb repulsion U and fully screened interaction W for Sc and Cu at different fillings with the different disentanglement schemes presented in Sec. II B.

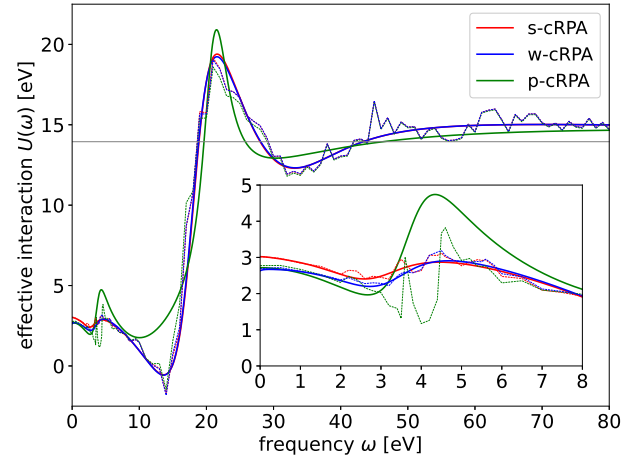


FIG. 3: (solid) Frequency dependence of effective interaction U for Sc⁴⁺ determined with various cRPA methods obtained from analytic continuation using a compressed Matsubara grid of 24 points.⁷⁶ For comparison data obtained from direct computation on the real-frequency axis is shown (dashed) Gray line corresponds to bare Coulomb interaction.

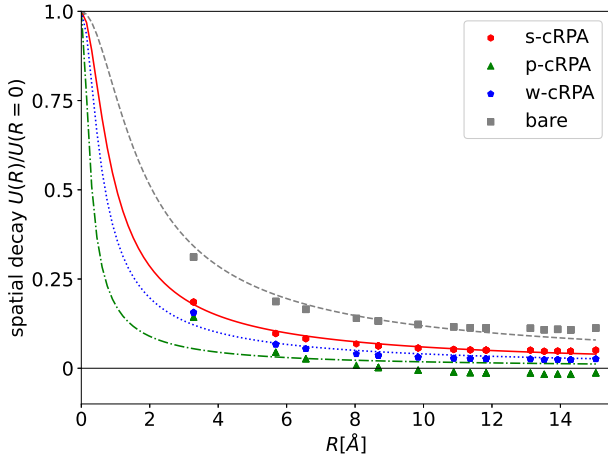


FIG. 4: Spatial decay of effective cRPA interactions scaled to one-site interaction $U(R)/U(R=0)$ for Sc^{4+} .

resolved well by the AAA fit.⁷⁷

All methods approach the bare Coulomb interaction (gray horizontal line) at high frequencies around 150 eV (not shown), but differ substantially at low frequencies. The inset shows the pronounced peak for p-cRPA at around 4.5 eV (green line) that is missing for w-cRPA and p-cRPA, but present for the fully screened interaction (not shown). Overall, s-cRPA and w-cRPA frequency dependence is similar, being almost constant at low frequencies and deviating substantially from the low-frequency regime of p-cRPA.

D. Spatial decay of Hubbard U

We shift the focus to the spatial decay of the effective cRPA interactions that is often described by the Ohno potential^{53,54}

$$\frac{U(R)}{U(R=0)} = \frac{1}{\sqrt{\frac{R}{\delta} + 1}}. \quad (23)$$

To this end, we have fitted this model to the calculated cRPA interactions

$$U_{\bar{\alpha}\bar{\beta}\bar{\gamma}\bar{\delta}} = \langle w_{\bar{\alpha}}, w_{\bar{\beta}} | \mathbf{U}(\omega=0) | w_{\bar{\gamma}}, w_{\bar{\delta}} \rangle, \quad (24)$$

restricted to two centres $\mathbf{R}_{\alpha} = \mathbf{R}_{\gamma} = \mathbf{R}$ and $\mathbf{R}_{\beta} = \mathbf{R}_{\delta} = 0$. The results are shown in Fig. 4. Overall, it can be seen that the cRPA interactions decay faster than the bare Coulomb interaction (squares). The Ohno model describes the decay of the s-cRPA interaction almost perfectly (hexagons), with slight deviations for w-cRPA for the nearest neighbor site (pentagons). Both, s-cRPA and w-cRPA approach each other with increasing distance. This is in contrast to p-cRPA. Judging from the figure, it seems that p-cRPA decays faster than the Ohno potential (triangles). However, trying to fit this behavior

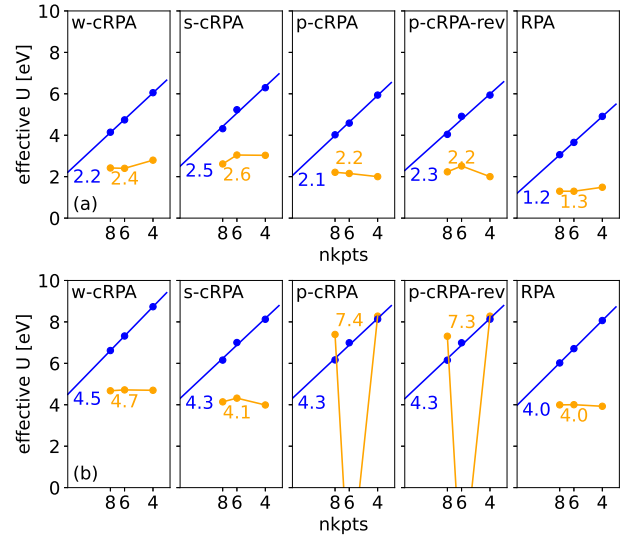


FIG. 5: On-site Hubbard-Kanamori parameter U (6) as a function of k-point sampling for each cRPA method studied, along with the fully screened interaction in RPA for Sc (a) and Cu (b). Each series contains four plots, one for each method. In every plot, the x-axis represents the number of k-points per direction used to sample the first Brillouin zone, and the y-axis shows the calculated U value. The blue line corresponds to data obtained without the long-wavelength limit correction; it exhibits a linear dependence on the inverse number of k-points, allowing for extrapolation to infinite k-point sampling.⁷⁰ The extrapolated interaction value is indicated as a blue number within each plot. The orange line shows results including the long-wavelength limit correction, with the value at an $8 \times 8 \times 8$ k-point grid represented by an orange number.

with another model is most probably misleading, since the interaction becomes negative around 8 Å. It can be expected that this unphysical behavior stems from the fact that this method violates particle number conservation and thus should be avoided in any cluster expansions of the model Hamiltonian.

E. k-point convergence

We analyze the k-point convergence of the effective interaction U by comparing results obtained without the long-wave limit correction, where U depends linearly on the inverse number of k-points used, as described in a recent study.⁷⁰ This linear dependence is illustrated in Fig. 5 (blue lines) for Sc and Cu across all cRPA methods considered, including the fully screened interaction, and allows extrapolation to infinite k-point sampling (blue numbers). Comparing these with the results that incorporate the $q \rightarrow 0$ limit (shown in orange) reveals that including this correction (Eq. 15) substantially improves k-point convergence in almost all cases. The main exceptions are the projector cRPA methods (p-cRPA and p-cRPA-rev) applied to Cu at a $6 \times 6 \times 6$ k-point mesh, where incorporating the long-wave limit leads to negative

TABLE III: Effectively screened, averaged on-site interaction U and exchange J of CaFeO_3 in localized (frontier) basis as calculated in Ref. 52.

| | p-cRPA | w-cRPA | s-cRPA |
|-----|-------------|-------------|-------------|
| U | 1.25 (1.75) | 0.45 (1.75) | 2.51 (1.90) |
| J | 0.92 (0.53) | 0.80 (0.53) | 0.97 (0.60) |

interaction values, rendering these approaches unreliable in practice. This is due to the violation of the positivity condition Eq. (18). In contrast, the w-cRPA and s-cRPA demonstrate markedly greater stability with respect to k-point sampling, comparable to that of the fully screened interaction. These latter two approaches converge more smoothly with the inclusion of the $q \rightarrow 0$ limit, making them more stable and dependable for practical use.

F. Effective interaction for CaFeO_3

Finally, we examined the averaged effective interaction for CaFeO_3 , as previously explored by Merkel and Ederer.⁵² In their recent study, they employed p-cRPA and w-cRPA methods—each within both localized and frontier basis sets—to determine the interaction parameters U and J for DFT+ U calculations. The precise definitions of these parameters, which differ from the Kanamori form used in Eq. (6), are detailed in their publication.⁵² In Table III, we present only the final s-cRPA results, alongside a comparison to the onsite and exchange interaction values reported by Merkel and Ederer for p-cRPA and w-cRPA, respectively. It is evident from these data that s-cRPA produces the largest interaction strengths among the considered methods. Nevertheless, even the onsite value of 2.51 eV predicted by s-cRPA would be insufficient for an accurate description of the $P2_1/n$ phase, as it would yield a metallic ground state with an almost vanishing R_1^+ mode. This is at odds with experimental observations, where an insulating phase stabilises, that is predicted with DFT+ U only within the range $4 \leq U \leq 7$ eV.⁵²

Achieving a more realistic value for U may require combining the strengths of s-cRPA with beyond RPA methods⁵¹ or alternative approaches such as the moment-constrained RPA method proposed by Spencer and Booth,⁸⁰ which both have shown promise in refining effective interaction parameters beyond standard cRPA.

IV. CONCLUSION

In conclusion, our comprehensive analysis of various constrained Random Phase Approximation (cRPA) methods applied to 3d transition metals reveals significant insights into their relative performance and applicability. The results consistently demonstrate that the spectral cRPA (s-cRPA) method offers the most robust

and physically meaningful approach for calculating effective interactions in these complex systems.

The s-cRPA method stands out by providing the largest effective interaction values among all methods studied, indicating its superior ability to capture the full extent of electronic correlations. Moreover, s-cRPA conserves electron number, a vital physical constraint that enhances the reliability of computed results. This method effectively removes most intra-d screening effects essential for accurately describing strongly correlated d-electrons within post mean-field theories. Additionally, s-cRPA implicitly incorporates off-diagonal elements of the correlated projector, resulting in a more complete and accurate electronic structure description.

Significantly, the application of s-cRPA to the realistic compound CaFeO_3 yields interaction parameters much closer to those required in DFT+ U calculations to correctly reproduce the experimentally observed insulating state. This highlights the practical advantage of s-cRPA for capturing the electronic correlations responsible for the gap formation in complex materials.

Furthermore, recent enhancements to our implementation enable calculation of multi-center interactions, allowing detailed study of the spatial decay of the screened Hubbard interaction U . We have also developed a low-scaling variant that utilizes a compressed Matsubara frequency grid, which facilitates efficient and accurate computation of the full frequency dependence of the effective interactions in large systems. This advancement opens new opportunities for studying the impact of defects on the effective interaction. Collectively, these developments enhance both the applicability and computational efficiency of s-cRPA.

These advantages make s-cRPA particularly well-suited for the study of transition metal systems and strongly correlated materials where precise electronic correlation treatment is paramount. Its consistent performance across a range of electron fillings and elements, combined with improved numerical stability over projector-based cRPA (especially in avoiding unphysical negative interactions), demonstrate its versatility and robustness.

Given these findings and methodological improvements, we strongly recommend adopting s-cRPA as the method of choice for calculating effective Hubbard interactions in transition metals and related strongly correlated systems. It provides more accurate, physically grounded, and computationally manageable results, which can enhance theoretical understanding and predictive capability in condensed matter physics and materials science.

Future work should focus on applying s-cRPA to a broader class of materials and comparing predictions with experimental data to further substantiate its superiority. Efforts to further optimize computational efficiency and incorporate additional physical effects will help ensure widespread adoption of s-cRPA within the scientific community.

Acknowledgments

Wannier transformation

Appendix A: Derivation of Eq. 12

A derivation of Eq. (12) starting from the Kubo formalism (11) can be found elsewhere.⁴⁴ Here, we derive Eq. (12) starting from the Wannier representation Eq. (10).⁸³ The expression is obtained by inserting the inverse

$$|\phi_{n\mathbf{k}}\rangle = \frac{1}{N_{\mathbf{k}}} \sum_{\alpha\mathbf{R}} e^{-i\mathbf{k}\mathbf{R}} T_{\alpha n}^*(\mathbf{k}) |w_{\alpha\mathbf{R}}\rangle \quad (\text{A1})$$

into Eq. (10) and performing the Fourier transformation to reciprocal space yielding

$$\begin{aligned} \chi_{\mathbf{G}\mathbf{G}'}^c(\mathbf{q}, \omega) = & \frac{1}{N_{\mathbf{k}}^2} \sum_{\bar{n}\bar{n}'} \frac{1}{N_{\mathbf{k}}^4} \sum_{\bar{n}_1\bar{n}_2\bar{n}_3\bar{n}_4} \frac{(1-f_{\bar{n}})f_{\bar{n}'}}{\epsilon_{\bar{n}} - \epsilon_{\bar{n}'} - \omega \mp i\eta} \langle \phi_{\bar{n}_1} | e^{i(\mathbf{G}+\mathbf{q})\mathbf{r}} | \phi_{\bar{n}_2} \rangle \langle \phi_{\bar{n}_3} | e^{-i(\mathbf{G}'+\mathbf{q})\mathbf{r}'} | \phi_{\bar{n}_4} \rangle \\ & \times \sum_{\alpha\beta\gamma\delta \in \mathcal{C}} T_{\alpha n}^*(\mathbf{k}) T_{\alpha n_1}(\mathbf{k}_1) T_{\beta n_2}^*(\mathbf{k}_2) T_{\beta n'}(\mathbf{k}') T_{\gamma n'}^*(\mathbf{k}') T_{\gamma n_3}(\mathbf{k}_3) T_{\delta n_4}^*(\mathbf{k}_4) T_{\delta n}(\mathbf{k}) \\ & \times \sum_{\mathbf{R}_{\alpha}} e^{i\mathbf{R}_{\alpha}(\mathbf{k}_1-\mathbf{k})} \sum_{\mathbf{R}_{\beta}} e^{-i\mathbf{R}_{\beta}(\mathbf{k}_2-\mathbf{k}')} \sum_{\mathbf{R}_{\gamma}} e^{i\mathbf{R}_{\gamma}(\mathbf{k}_3-\mathbf{k}')} \sum_{\mathbf{R}_{\delta}} e^{-i\mathbf{R}_{\delta}(\mathbf{k}_4-\mathbf{k})}, \quad \bar{n}_i = (n_i, \mathbf{k}_i). \end{aligned} \quad (\text{A2})$$

This expression simplifies to Eq. (12) after using⁸¹

$$\sum_{\mathbf{R}} e^{i\mathbf{k}\mathbf{R}} = \sum_{\mathbf{G}} \delta_{\mathbf{k}\mathbf{G}} \quad (\text{A3})$$

and the periodicity condition⁵⁷

$$T_{n\alpha}^{(\mathbf{k})} = T_{n\alpha}^{(\mathbf{k}+\mathbf{G})} \quad (\text{A4})$$

eigenvalues are discrete and either 0 or 1. This enables direct identification of the singular eigenvectors. The left singular vectors U correspond to the selected row vectors of the Wannier projection matrix T , while the right singular vectors V correspond to selected column vectors of T^\dagger . This structure has an important consequence when combining Eq. (20) with Eq. (14). The leverage scores appear directly as the diagonal elements in P .

Appendix B: Leverage score

The matrix P defined in Eq. (14) is a projector and thus idempotent, i.e. $P^\dagger P = P$. As a consequence the

References

- ¹ J. C. Slater, Phys. Rev. **36**, 57 (1930), URL <https://doi.org/10.1103/PhysRev.36.57>.
- ² H. Bethe, Zeitschrift für Physik **71**, 205 (1931), URL <https://doi.org/10.1007/BF01341708>.
- ³ N. F. Mott, Proceedings of the Physical Society. Section A **62**, 416 (1949), URL <https://dx.doi.org/10.1088/0370-1298/62/7/303>.
- ⁴ J. Hubbard, Royal Society of London Proceedings Series A **276**, 238 (1963), URL <https://doi.org/10.1098/rspa.1963.0204>.
- ⁵ N. Mott, Advances in Physics **13**, 325 (1964), URL <https://doi.org/10.1080/00018736400101041>.
- ⁶ N. F. Mott, Rev. Mod. Phys. **40**, 677 (1968), URL <https://doi.org/10.1103/RevModPhys.40.677>.
- ⁷ Y. Nagaoka, Phys. Rev. **147**, 392 (1966), URL <https://doi.org/10.1103/PhysRev.147.392>.
- ⁸ M. C. Gutzwiller, Phys. Rev. **137**, A1726 (1965), URL <https://doi.org/10.1103/PhysRev.137.A1726>.
- ⁹ N. Andrei, Phys. Rev. Lett. **45**, 379 (1980), URL <https://doi.org/10.1103/PhysRevLett.45.379>.
- ¹⁰ A. Georges, G. Kotliar, K. W., and M. J. Rozenberg, Rev. Mod. Phys. **68**, 13 (1996), URL <https://doi.org/10.1103/RevModPhys.68.13>.
- ¹¹ W. Metzner and D. Vollhardt, Phys. Rev. Lett. **62**, 324 (1989), URL <https://doi.org/10.1103/PhysRevLett.62.324>.
- ¹² P. W. Anderson, Phys. Rev. **124**, 41 (1961), URL <https://doi.org/10.1103/PhysRev.124.41>.
- ¹³ A. Georges and G. Kotliar, Phys. Rev. B **45**, 6479 (1992).
- ¹⁴ A. Georges and W. Krauth, Phys. Rev. Lett. **69**, 1240 (1992), URL <https://doi.org/10.1103/PhysRevB.45.6479>.
- ¹⁵ P. Werner, A. Comanac, L. de Medici, M. Troyer, and A. J. Millis, Phys. Rev. Lett. **97**, 076405 (2006), URL <https://doi.org/10.1103/PhysRevLett.97.076405>.
- ¹⁶ N. Blümer, Phys. Rev. B **76**, 205120 (2007), URL <https://doi.org/10.1103/PhysRevB.76.205120>.
- ¹⁷ D. Rost, F. Assaad, and N. Blümer, Phys. Rev. E

- 87**, 053305 (2013), URL <https://doi.org/10.1103/PhysRevE.87.053305>.
- ¹⁸ N. Parragh, A. Toschi, K. Held, and G. Sangiovanni, Phys. Rev. B **86**, 155158 (2012), URL <https://doi.org/10.1103/PhysRevB.86.155158>.
 - ¹⁹ K. Held, I. A. Nekrasov, G. Keller, V. Eyert, N. Blümer, A. K. McMahan, R. T. Scalettar, T. Pruschke, V. I. Anisimov, and D. Vollhardt, physica status solidi (b) **243**, 2599 (2006), URL <https://doi.org/10.1002/pssb.200642053>.
 - ²⁰ K. Held, O. K. Andersen, M. Feldbacher, A. Yamasaki, and Y.-F. Yang, Journal of Physics: Condensed Matter **20**, 064202 (2008), URL <https://dx.doi.org/10.1088/0953-8984/20/6/064202>.
 - ²¹ G. Kotliar, S. Y. Savrasov, K. Haule, V. S. Oudovenko, O. Parcollet, and C. A. Marianetti, Rev. Mod. Phys. **78**, 865 (2006), URL <https://link.aps.org/doi/10.1103/RevModPhys.78.865>.
 - ²² M. B. Zöhl, I. A. Nekrasov, T. Pruschke, V. I. Anisimov, and J. Keller, Phys. Rev. Lett. **87**, 276403 (2001), URL <https://doi.org/10.1103/PhysRevLett.87.276403>.
 - ²³ A. I. Lichtenstein, M. I. Katsnelson, and G. Kotliar, Phys. Rev. Lett. **87**, 067205 (2001), URL <https://doi.org/10.1103/PhysRevLett.87.067205>.
 - ²⁴ E. Pavarini, A. Yamasaki, J. Nuss, and O. K. Andersen, New Journal of Physics **7**, 188 (2005), URL <https://dx.doi.org/10.1088/1367-2630/7/1/188>.
 - ²⁵ C. Taranto, M. Kaltak, N. Parragh, G. Sangiovanni, G. Kresse, A. Toschi, and K. Held, Phys. Rev. B **88**, 165119 (2013), URL <https://doi.org/10.1103/PhysRevB.88.165119>.
 - ²⁶ A. Floris, I. Timrov, B. Himmetoglu, N. Marzari, S. de Gironcoli, and M. Cococcioni, Phys. Rev. B **101**, 064305 (2020), URL <https://link.aps.org/doi/10.1103/PhysRevB.101.064305>.
 - ²⁷ J.-J. Zhou, J. Park, I. Timrov, A. Floris, M. Cococcioni, N. Marzari, and M. Bernardi, Phys. Rev. Lett. **127**, 126404 (2021), URL <https://link.aps.org/doi/10.1103/PhysRevLett.127.126404>.
 - ²⁸ A. Floris, S. de Gironcoli, E. K. U. Gross, and M. Cococcioni, Phys. Rev. B **84**, 161102 (2011), URL <https://link.aps.org/doi/10.1103/PhysRevB.84.161102>.
 - ²⁹ A. Carta, I. Timrov, S. Beck, and C. Ederer, *Bridging constrained random-phase approximation and linear response theory for computing hubbard parameters* (2025), 2505.03698, URL <https://arxiv.org/abs/2505.03698>.
 - ³⁰ S. Biermann, F. Aryasetiawan, and A. Georges, Phys. Rev. Lett. **90**, 086402 (2003), URL <https://doi.org/10.1103/PhysRevLett.90.086402>.
 - ³¹ F. Aryasetiawan, M. Imada, A. Georges, G. Kotliar, S. Biermann, and A. I. Lichtenstein, Phys. Rev. B **70**, 195104 (2004), URL <https://doi.org/10.1103/PhysRevB.70.195104>.
 - ³² F. Aryasetiawan, K. Karlsson, O. Jepsen, and U. Schönberger, Phys. Rev. B **74**, 125106 (2006), URL <https://doi.org/10.1103/PhysRevB.74.125106>.
 - ³³ A. Kutepov, K. Haule, S. S. Y., and G. Kotliar, Phys. Rev. B **82**, 045105 (2010), URL <https://doi.org/10.1103/PhysRevB.82.045105>.
 - ³⁴ Y. Nomura, M. Kaltak, K. Nakamura, C. Taranto, S. Sakai, A. Toschi, R. Arita, K. Held, G. Kresse, and M. Imada, Phys. Rev. B **86**, 085117 (2012).
 - ³⁵ T. Miyake, F. Aryasetiawan, and M. Imada, Phys. Rev. B **80**, 155134 (2009).
 - ³⁶ T. Miyake and F. Aryasetiawan, Phys. Rev. B **77**, 085122 (2008), URL <https://doi.org/10.1103/PhysRevB.77.085122>.
 - ³⁷ E. Şaşıoğlu, C. Friedrich, and S. Blügel, Phys. Rev. B **83**, 121101 (2011), URL <https://doi.org/10.1103/PhysRevB.83.121101>.
 - ³⁸ W. Z. B. Shih, Y. Zhang and P. Zhang, Phys. Rev. B **85**, 045132 (2012), URL <https://doi.org/10.1103/PhysRevB.85.045132>.
 - ³⁹ B. Amadon, T. Applencourt, and F. Bruneval, Phys. Rev. B **89**, 125110 (2014), URL <https://doi.org/10.1103/PhysRevB.89.125110>.
 - ⁴⁰ K. Nakamura, Y. Yoshimoto, Y. Nomura, T. Tadano, M. Kawamura, T. Kosugi, K. Yoshimi, T. Misawa, and Y. Motoyama, Computer Physics Communications **261**, 107781 (2021).
 - ⁴¹ *The fleur project*, URL <https://www.flapw.de>.
 - ⁴² R. Sakuma and F. Aryasetiawan, Phys. Rev. B **87**, 165118 (2013), URL <https://doi.org/10.1103/PhysRevB.87.165118>.
 - ⁴³ H. J. L. Vaugier and S. Biermann, Phys. Rev. B **86**, 165105 (2012), URL <https://doi.org/10.1103/PhysRevB.86.165105>.
 - ⁴⁴ M. Kaltak, *Merging GW with DMFT* (University of Vienna, 2015), URL <https://theses.univie.ac.at/detail/33771#>.
 - ⁴⁵ A. Hampel, P. Liu, C. Franchini, and C. Ederer, npj Quantum Materials **4**, 5 (2019), URL <https://doi.org/10.1038/s41535-019-0145-4>.
 - ⁴⁶ J. Karp, A. Hampel, and A. J. Millis, Phys. Rev. B **103**, 195101 (2021), URL <https://link.aps.org/doi/10.1103/PhysRevB.103.195101>.
 - ⁴⁷ L. Muechler, D. I. Badrtdinov, A. Hampel, J. Cano, M. Rösner, and C. E. Dreyer, Phys. Rev. B **105**, 235104 (2022), URL <https://link.aps.org/doi/10.1103/PhysRevB.105.235104>.
 - ⁴⁸ A. Hampel, J. Lee-Hand, A. Georges, and C. E. Dreyer, Phys. Rev. B **104**, 035102 (2021), URL <https://link.aps.org/doi/10.1103/PhysRevB.104.035102>.
 - ⁴⁹ H. Chen, A. Hampel, J. Karp, F. Lechermann, and A. J. Millis, Frontiers in Physics **10** (2022), URL <https://www.frontiersin.org/journals/physics/articles/10.3389/fphy.2022.835942>.
 - ⁵⁰ D. I. Badrtdinov, C. Rodriguez-Fernandez, M. Grzeszczyk, Z. Qiu, K. Vaklinova, P. Huang, A. Hampel, K. Watanabe, T. Taniguchi, L. Jiong, et al., Small **19**, 2300144 (2023), URL <https://onlinelibrary.wiley.com/doi/abs/10.1002/sml.202300144>.
 - ⁵¹ E. G. C. P. van Loon, M. Rösner, M. I. Katsnelson, and T. O. Wehling, Phys. Rev. B **104**, 045134 (2021), URL <https://link.aps.org/doi/10.1103/PhysRevB.104.045134>.
 - ⁵² M. E. Merkel and C. Ederer, Phys. Rev. Res. **6**, 013230 (2024), URL <https://link.aps.org/doi/10.1103/PhysRevResearch.6.013230>.
 - ⁵³ D. Di Sante, B. Kim, W. Hanke, T. Wehling, C. Franchini, R. Thomale, and G. Sangiovanni, Phys. Rev. Res. **5**, L012008 (2023), URL <https://link.aps.org/doi/10.1103/PhysRevResearch.5.L012008>.
 - ⁵⁴ I. R. Reddy, C.-J. Kang, S. Kim, and B. Kim, npj Computational Materials **10**, 286 (2024), URL <https://doi.org/10.1038/s41524-024-01454-9>.
 - ⁵⁵ W. Kohn, Phys. Rev. B **7**, 4388 (1973), URL <https://doi.org/10.1103/PhysRevB.7.4388>.

- ⁵⁶ C. Brouder, G. Panati, M. Calandra, C. Mourougane, and N. Marzari, Phys. Rev. Lett. **98**, 046402 (2007), URL <https://doi.org/10.1103/PhysRevLett.98.046402>.
- ⁵⁷ N. Marzari, A. A. Mostofi, J. R. Yates, I. Souza, and D. Vanderbilt, Rev. Mod. Phys. **84**, 1419 (2012), URL <https://doi.org/10.1103/RevModPhys.84.1419>.
- ⁵⁸ N. Marzari and D. Vanderbilt, Phys. Rev. B **56**, 12847 (1997), URL <https://doi.org/10.1103/PhysRevB.56.12847>.
- ⁵⁹ E. Şaşıoğlu, A. Schindlmayr, C. Friedrich, F. Freimuth, and S. Blügel, Phys. Rev. B **81**, 054434 (2010), URL <https://link.aps.org/doi/10.1103/PhysRevB.81.054434>.
- ⁶⁰ A. A. Mostofi, J. R. Yates, Y.-S. Lee, I. Souza, D. Vanderbilt, and M. N., Comp. Phys. Comm. **178**, 685 (2008), URL <https://www.sciencedirect.com/science/article/pii/S0010465507004936>.
- ⁶¹ E. Pavarini, E. Koch, D. Vollhardt, and A. E. . Lichtenstein, *The LDA+DMFT approach to strongly correlated materials: lecture notes of the autumn school 2011, hands-on LDA+DMFT; autumn school organized by the DFG research unit 1346 dynamical mean-field approach with predictive power for strongly correlated materials at Forschungszentrum Jülich 4-7 October 2011* (Forschungszentrum, Zentralbibliothek, 2011), URL <http://hdl.handle.net/2128/4467>.
- ⁶² S. Adler, Phys. Rev. **126**, 413 (1962), URL <https://link.aps.org/doi/10.1103/PhysRev.126.413>.
- ⁶³ N. Wiser, Phys. Rev. **129**, 62 (1963), URL <https://link.aps.org/doi/10.1103/PhysRev.129.62>.
- ⁶⁴ R. Starke, *Quantum Field Theoretical Green Functions and Electronic Structure* (University of Vienna, 2012), URL <https://theses.univie.ac.at/detail/19589>.
- ⁶⁵ A. L. Fetter and J. D. Walecka, *Quantum theory of many-particle systems*, Dover Books on Physics (Dover Publications, 2003), URL <https://archive.org/details/quantum-theory-of-many-particle-systems-by-alexander-fetter-john-dirk-walecka-physics-z-lib.org>.
- ⁶⁶ C. Ambrosch-Draxl and J. O. Sofo, Computer Physics Communications **175**, 1 (2006), URL <https://www.sciencedirect.com/science/article/pii/S0010465506001299>.
- ⁶⁷ M. Gajdoš, K. Hummer, G. Kresse, J. Furthmüller, and F. Bechstedt, Phys. Rev. B **73**, 045112 (2006).
- ⁶⁸ G. James, D. Witten, T. Hastie, and R. Tibshirani, *An Introduction to Statistical Learning: with Applications in R*, Springer Texts in Statistics (Springer New York, 2013), ISBN 9781461471387, URL https://books.google.at/books?id=qcI_AAAAQBAJ.
- ⁶⁹ P. Drineas, M. Magdon-Ismael, M. W. Mahoney, and D. P. Woodruff, J. Mach. Learn. Res. **13**, 3475–3506 (2012), URL <https://dl.acm.org/doi/10.5555/2503308.2503352>.
- ⁷⁰ I. R. Reddy, M. Kaltak, and B. Kim, Phys. Rev. B **111**, 195144 (2025), URL <https://link.aps.org/doi/10.1103/PhysRevB.111.195144>.
- ⁷¹ J.-F. Cardoso and A. Souloumiac, SIAM J. Mat. Anal. Appl. **17**, 161 (1996), URL <https://www.sciencedirect.com/science/article/pii/S0010465507004936>.
- ⁷² W. H. Press, S. A. Teukolsky, W. T. Vetterling, and B. P. Flannery, *Numerical Recipes 3rd Edition: The Art of Scientific Computing* (Cambridge University Press, 2007).
- ⁷³ M. W. Mahoney and P. Drineas, Proceedings of the National Academy of Sciences **106**, 697 (2009), URL <https://www.pnas.org/doi/abs/10.1073/pnas.0803205106>.
- ⁷⁴ LMAXFOCKAE vasp wiki entry, URL https://www.vasp.at/wiki/index.php/NMAXFOCKAE_and_LMAXFOCKAE.
- ⁷⁵ A. R. Altman, S. Kundu, and F. H. da Jornada, Phys. Rev. Lett. **132**, 086401 (2024), URL <https://link.aps.org/doi/10.1103/PhysRevLett.132.086401>.
- ⁷⁶ M. Kaltak and G. Kresse, Phys. Rev. B **101**, 205145 (2020), URL <https://link.aps.org/doi/10.1103/PhysRevB.101.205145>.
- ⁷⁷ Y. Nakatsukasa, O. Sète, and L. N. Trefethen, SIAM Journal on Scientific Computing **40**, A1494 (2018), URL <https://doi.org/10.1137/16M1106122>.
- ⁷⁸ py4vasp, URL <https://vasp.at/py4vasp/latest>.
- ⁷⁹ G. Kresse and D. Joubert, Phys. Rev. B **59**, 1758 (1999).
- ⁸⁰ C. J. C. Scott and G. H. Booth, Phys. Rev. Lett. **132**, 076401 (2024), URL <https://link.aps.org/doi/10.1103/PhysRevLett.132.076401>.
- ⁸¹ G. Czycholl, *Theoretische Festkörperphysik: Von Den Klassischen Modellen Zu Modernen Forschungsthemen* (Springer, 2004).
- ⁸² W. Hanke and L. J. Sham, Phys. Rev. B **21**, 4656 (1980), URL <https://link.aps.org/doi/10.1103/PhysRevB.21.4656>.
- ⁸³ Eq. (10) is the constrained version of full RPA polarizability in Wannier basis originally derived by Hanke and Sham⁸².